Effects of a Three-Dimensional-Printed Atomizer Component on Fuel-Spray and Flame Characteristics of a Jet-Stabilized Compact Gas Turbine Combustor Fed with Liquid Fuels

Haisol Kim[1]
German Aerospace Center (DLR)
Pfaffenwaldring 38-40, 70569 Stuttgart, Germany
Haisol.Kim@dlr.de

Jhon Pareja
German Aerospace Center (DLR)
Pfaffenwaldring 38-40, 70569 Stuttgart, Germany
Jhon.ParejaRestrepo@dlr.de

Oliver Lammel
German Aerospace Center (DLR)
Pfaffenwaldring 38-40, 70569 Stuttgart, Germany
Oliver.Lammel@dlr.de

ABSTRACT

In this work, the effects of replacing an atomizer component of a confined jet-stabilized gas turbine combustor with a 3D-printed part have been studied. The part is called airblast, and it serves as a wall that collects and flows liquid droplets for a secondary atomization. Therefore, the liquid-surface interaction on the rough surface of the 3D-printed part was of interest.

The combustor was operated under various conditions with either a conventionally machined airblast or the 3D-printed airblast. Flames with two liquid fuels were studied for fuel flexibility, and the position of a primary fuel injection was varied to study the influence of the liquid-surface interaction length. Load

[1] email: haisol.kim@dlr.de

flexibility was investigated with air jet velocity settings, and flame equivalence ratios of ϕ=0.8 and 1.0 were tested.

Shadowgraphy-based particle tracking analyses presented a reduced atomization performance with the 3D-printed airblast, showing large droplet size distributions. However, no significant change in the combustor performance was observed from OH chemiluminescence images and emission data, which confirms the versatility of the combustor and assures the compatibility of 3D-printed components with the combustor of this study.*

1. INTRODUCTION

Micro gas turbines (MGTs) serve as a promising alternative for decentralized power generation with high power density, fuel flexibility, and low emissions [1]. Gas turbines can be operated with either gaseous or liquid fuels [1, 2], and liquid energy carriers will play an essential role in energy transition systems because they provide high energy density which can bring advantages in autonomy, transportation, and storage. MGTs have the potential to operate with a variety of alternative and renewable liquid fuels produced from various sources (i.e., various compositions and properties), without major technical modifications. However, when operating MGTs with liquid fuels, an atomization system is required [2], and it increases the challenges of scalability, mainly regarding proper mixing of fuel and oxidizer within short time scales.

Recently, a canonical single-nozzle confined burner fed by liquid fuels was developed, employing a high-momentum jet stabilization technology [3]. The burner was developed with a focus on MGT applications, and it includes a novel in-house dual pressure swirl atomizer (PSA)/airblast injection concept. The PSA produces a fuel spray, and the large droplets of the spray are collected and re-atomized by high shear forces on the wall of an airblast. The evaluation of the burner showed that high operational and thermal load flexibility is achieved with low emissions when using extra light heating oil (HEL) as fuel [3].

One additional challenge with small-scale liquid injection systems lies in the manufacture of the components. Parts with complex geometries are often required, which results in long production times and high costs. In this regard, additive manufacturing of metal components (so-called metal 3D printing), in particular laser powder bed fusion (LPBF or selective laser melting, SLM), has gained relevance in the low-cost fast prototyping and production of gas turbine components [4, 5] including injections systems [6-8]. However, due to the powder-melting and layer-by-layer building process, the surface quality of 3D-printed metal components is often a matter of concern in liquid-surface interactions.

In recent studies by Cejpek et al. and Jedelský et al. [9, 10], the effects of the surface roughness on the atomization performance of 3D-printed pressure swirl atomizers were evaluated. However, the 3D-printed components had to be fabricated on a large scale due to the size limitation of the available SLM technique. It was concluded in those studies that large surface roughness and manufacturing imperfections can worsen the spray quality, e.g., spray distribution uniformity, based on the evaluation with the up-scaled printed atomizer.

Sanchez et al. compared the atomization performance of 3D-printed and conventionally machined airblast-atomization systems, which resembles typical RQL

(Rich-Quench-Lean) aviation combustors (i.e., fuel channels with integrated inner air swirlers) [7]. It was shown that the functional behavior of the 3D-printed injector matches the reference part with very little differences. Crayford et al. evaluated a 3D-printed pre-filming airblast atomization system produced by SLM and electro-polished afterward to improve the surface quality [11]. A uniform spray was generated, although the pressure drop of the airflow through the injector was around 30% larger than predicted. Nevertheless, combustion experiments at atmospheric pressure with Jet A-1 demonstrated flame stability across a wide range of operating conditions.

Conclusions from the previous works impose a necessity of studying 3D-printed parts to further develop burners with desired geometry at lower cost. Therefore, in this work, the machined airblast of the dual injection system of the confined jet-stabilized burner in the previous work was replaced by a 3D-printed component to investigate its impact on the burner's performance [3]. Atomization quality, flame characteristics, and exhaust gas composition were compared for the 3D-printed and conventionally machined airblasts installed in the burner. The experiments were performed at comprehensive operating conditions, using Jet A-1 and HEL as fuel.

2. MATERIALS AND METHODS

2.1. Confined jet-stabilized burner

The design and development of the single-nozzle jet-stabilized burner for liquid fuels have been described in the previous work [3], so it will be briefly introduced here. A schematic of the burner assembly on an atmospheric pressure test rig is depicted in Fig. 1. The combustion chamber has a rectangular cross-section of 40 × 50 mm^2 with a total length of 600 mm consisting of three segments providing excellent optical access (only one of the segments is shown in Fig. 1a). The burner nozzle has an inner diameter of 12 mm and is placed off-centered along one of the axes to stabilize the flame by recirculation [12]. Preheated air at a controlled flow rate and temperature is supplied to the burner. The high-momentum air flow is conditioned through a contoured contraction nozzle which is coaxial to a fuel lance. The fuel lance supplies fuel, and it is water-cooled. A pressure swirl atomizer (PSA) is mounted at the tip of the fuel lance. Throughout this study, a PSA with a flow number of 0.35 was employed. The flow number is defined according to Lefebvre and McDonell [13], as:

$$FN_{\mathrm{US}} = \frac{\text{Flow rate, lb/h}}{(\text{Injection pressure differential, psid})^{0.5}} \quad (1)$$

The detailed pressure swirl atomizer-airblast injection system is presented in Fig. 1b. When a fuel spray is generated by the PSA, small droplets are transported by high-momentum air jet directly into the combustion chamber, while large droplets and ligaments that flow radially are collected by the airblast and re-atomized by shear forces at the exit. The position and design of the airblast create a geometric split of the entire air flow into atomization and co-flow air [3]. Depending on how the mixing length (l_m) is set, the fuel and air can continue mixing inside the nozzle or the mixture can directly enter the combustion chamber. l_m was kept at 0 in this study. The axial position of the PSA with respect to the airblast can vary the film length, l_f, by changing the fixing position of the fuel lance.

2.2. 3D-printed airblast

Fig. 2 presents a 3D model of the airblast. The airblast was printed as a single part by SLM using a metal 3D printer (EOS M290) in layers of 40 µm of stainless steel (316L/1.4404). As illustrated in Fig. 2, some surfaces for sealing were polished after being printed, to improve their surface roughness (Ra = 4-7 µm). On the other hand, the surfaces in contact with the fuel and air flows have kept the surface roughness of the SLM process (Ra = ~35 µm). The surface roughness difference is distinct from the microscopic images.

2.3. Operating conditions

In order to study the effects of the 3D-printed component on the burner system, multiple parameters were varied for the tests with both the machined airblast and the 3D-printed airblast: liquid fuel, injector (PSA) position, air jet velocity, and equivalence ratio (ϕ). Jet A-1 and HEL were chosen as liquid fuels, and injection from the PSA was at either one diameter (i.e., 1d=12 mm) or two times the diameter below the nozzle tip. Air jet velocity (i.e., bulk velocity) was set to 120 or 160 m/s. ϕ = 0.8 was set as a reference value, while ϕ = 1.0 was tested for some limited cases. The combinations of the variable parameters are listed in Table 1, and case numbers are assigned for each airblast type as a reference. Other parameters, such as mixing length l_m=0 (cf. Fig. 1b) and the air preheating temperature of 650 K were kept for all cases.

2.4. Shadowgraphy, chemiluminescence imaging, and emission measurement

The atomization process was evaluated at different locations downstream in the burner using double-pulse background-illuminated shadowgraphy. For the double-pulse illumination, two second-harmonic laser beams from two identical Nd:YAG lasers

(Quanta Ray, Spectra Physics) were expanded to a diameter of 150 mm using a spherical lens (*f*=30 mm) and utilized to induce light emission from a fluorescence screen (diffused red-shifted light, decay time <50 ns). The time interval between two pulses was set to 2 µs. A CMOS camera (LaVision CX12) was employed for the imaging, with a 180 mm macro lens of f/2.8 (Sigma). The field of view was set to 15 x 20 mm^2, and the size of one pixel in the shadowgraphy image was equivalent to 5 µm. By translating the burner, six heights in steps of 18 mm in the axial direction were measured, and the heights were covering from the nozzle exit to the lower part of the flames. At each height, 300 instantaneous double-frame images were recorded at 10 Hz, with a frame Δt of 2 µs.

High-speed OH* chemiluminescence (*CL*) imaging at 14 kHz was simultaneously employed to study flame behaviors since an OH* *CL* signal indicates where heat release zones are located. A high-speed camera (Photron FASTCAM SA5) coupled with high-speed intensified relay optics (LaVision HS-IRO). A 64 mm f/2.0 UV lens (Halle Nachfl.) and a 310-320 nm band-pass filter (AHF) were used to collect the OH* signal. The *CL* images were taken from the side perpendicular to the shadowgraphy imaging, and therefore, the off-centered flame and recirculation zone could be visualized in the images. The field of view was set to 100 x 200 mm^2, which covers one section of the combustion chamber (cf. Fig. 1). *CL* images presented in this study were taken at the bottom section (i.e., nozzle height) of the burner.

Exhaust gas composition was measured using a portable reference emission analyzer (MRU MGA prime), using its probe installed at the top of the combustion chamber (i.e., 600 mm above the nozzle). The probe was air-cooled to prohibit further reaction in the tube, and the gas was kept heated up to the gas analyzer to prevent water condensation during the transportation. The air-cooling amount was adjusted depending on the flame conditions, and the tube-heating temperature was kept at 120°C.

2.5. Particle tracking velocimetry

A sample shadowgraphy image from the lowest height is presented in Fig. 3, overlaid by detected droplets and computed vectors. Particle detecting, sizing, and linking between two frames of a shadowgraphy image were done with the help of the Python toolbox Trackpy (version 0.6.1) [14, 15]. Raw images were pre-processed by flat background removal and gradient mapping, which provided the best-binarized results. In the next step, the Trackpy algorithm linked the particles by iteration based on the initial velocity input (i.e., air jet velocity) and the size similarity. At last, velocity components were calculated based on the displacement, and the axial velocity component and size of detected particles were analyzed. The minimum size of detection was set to 3 pixels, and it is equivalent to a spherical droplet with a diameter of 9.8 μm.

For the analysis between different cases, droplet size distributions, instead of averaged absolute sizes, are compared. This is due to the limitation regarding the depth of field. The detected particles are accumulated along the lens axis for a certain distance (i.e., focal depth) and the droplet sizes are overestimated due to the particles slightly out of focus. A depth of field calibration can be useful to compensate this effect, but it was not possible to obtain reference images with the same temperature gradient as in an operating burner. Therefore, processing the droplet size information further into a single representing value and comparing them between cases could lead to a biased conclusion.

3. RESULTS AND DISCUSSION

In Fig. 4, as an example, axial velocity-size relations of the detected droplets are presented for two cases using the machined airblast. All the detected droplets from 300 images of the same height are marked with one color, and six colors are used for the six heights. An axial velocity component, computed from an apparent displacement on the images, is used for the analyses due to the lack of three-dimensional information. Droplet size analysis is based on a sphere-equivalent diameter to compare the droplets in different shapes. Droplet sizes are discrete due to the conversion from the pixel counting, and it is more visible for the small values (cf. left part of Fig. 4).

Mean curves of the droplets at all heights are added in Fig. 4. Due to the discrete manner of the droplet sizes, group mean velocities for each size could be easily computed. On the other hand, velocities had to be grouped arbitrarily with a step of 5 m/s to compute group mean sizes. Using these values, group mean velocity curves were drawn horizontally, and group mean size curves were drawn vertically in both panels. When the data points are insufficient in quantity, a fluctuation in the mean curves is observed. Therefore, the large noise level of the mean curves indicates small population of droplets at the part of the plot (cf. right side of Fig. 4).

The entire data set from cases 1 to 20 has been thoroughly investigated using scatter plots and raw images, and some distinct tendencies were observed. For more detailed analyses, group mean curves at each measurement height are presented in Fig. 5. For better visibility, individual markers are removed and mean curves for each height are drawn in Fig. 5, with the same color code used in Fig. 4.

In Fig. 5, a clear difference between 120 and 160 m/s air jet velocity cases is observed. The mean axial velocity is naturally larger for 160 m/s case for all the heights, and the air jet velocity presents an impact on the droplet size distribution. Looking at the vertical curves in Fig. 5a, droplets tend to be more populated at certain axial velocity, and thus some peaks appear. In addition, the peak position shifts to a larger axial velocity as the height increases. It implies that there is a dominant size group of droplets that accelerates with the airflow. The grouping is not very pronouncing close to the nozzle possibly due to the large number of droplets in a wide range of sizes, but the grouping is trackable from the height 36 mm above the nozzle (cf. the green curve in Fig. 5a) and higher. On the other hand, no dominant droplet size group is observed from the 160 m/s air jet velocity case (cf. Fig. 5b). It shows quite even droplet size distribution, and it is only noticeable that the overall droplet size is larger for the lowest height than the other heights.

To compare different cases in a straightforward way, the group mean size curves (i.e., vertical curves in Fig. 5) are drawn together with reduced complexity. A contour of the full outer join area for each case is introduced, and the detailed process of making a contour is illustrated in Fig. 6. By using these size contours, the overall size distribution of each case can be directly compared without losing the height-specific information.

The results from all the cases in Table 1 are presented in Fig. 7, where four size contours are presented in each panel and compared. In each panel, three variable parameters (cf. Table 1) are shared and noted at the upper right corner. The other two variables are labeled next to each curve, after their case number and followed by the total number of droplets detected. In this way, all the cases in Table 1 could be compared relatively straightforward. For an easier data comparison for the readers, shades of red or yellow colors are used to present the cases with the 3D-printed airblast, while the other colors are with the machined airblast. In addition, a few cases appear again in another panel, and they keep the same colors.

In Fig. 7, a few general tendencies are found when cases with different airblasts or air jet velocities are compared. The 3D-printed airblast results in larger numbers of droplets detected from 30% to 120% more than the machined airblast cases (cf. the numbers at the end of each label in Fig. 7) for all cases except one pair (i.e., case 5 and 15 in panel a). Regarding the number of droplets detected, efficient atomization and evaporation of liquid fuel would reduce the number of detectible droplets in the vicinity of a flame. On the other hand, the larger number of droplets could mean good atomization as well, if the droplet sizes are smaller. Therefore, the number of droplets has to be interpreted together with the mean droplet size for each case. In general, most of the cases in Fig. 7 present pronounced droplet number increase accompanied by mean size increase, which supports that the 3D-printed airblast produces larger droplets as a result of a less efficient atomization performance.

As discussed earlier in Fig. 5, the flatness of a group mean velocity curve is correlated to the air jet velocity, and the trend is shown in Fig. 7a, 7b, and 7e. 120 m/s setting tends to present distinct peak sizes at certain velocities, but peaks are less pronounced for 160 m/s cases. There are two cases that do not follow this general trend, namely, cases 15 and 20 in Fig. 7a and 7b, respectively. Both cases are with the 3D-printed airblast and the injector positioned at 2d. Therefore, it implies that the presence of the dominant size group is related to the interaction between the surface of the airblast and the liquid fuel. From the observation, a rougher surface of the wall and a longer interaction between the wall and the liquid are represented by the peaks in the velocity-size plot. However, further investigation is necessary to understand the detailed physics of the phenomenon.

The effect of different airblast types can be studied using Fig. 7a and 7b as well. On average, 3D-printed airblast forms larger droplets than the machined airblast. When the machined airblast is employed, Jet A-1 results in a smaller mean droplet size than HEL. However, with the 3D-printed airblast, smaller mean droplet sizes are measured from the HEL cases than the Jet A-1 cases. Therefore, the largest differences in the mean droplet sizes are observed from the pair of cases 3-13 (cf. in Fig. 7a).

When the PSA is moved downstream (from 2d to 1d position) the deviation between different airblasts becomes smaller. They are compared in Fig. 7c and 7d with the previous pairs of cases 3-13 and 8-18, respectively. If we look at the individual contours in panels c and d closely, two contours on the left side of each panel show similar mean droplet size values, but the other two on the right are deviated. In other words, whether the injector is located at 1d or 2d is not critical for the machined airblast, but for the 3D-printed airblast, it results in a poorer atomization when the contact length between liquid fuels and the airblast gets longer. The decreasing number of droplets detected for the 2d cases (cf. cases 13 and 18 in Fig. 7c and 7d, respectively) also supports the less efficient atomization of the 3D-printed airblast combined with the injector at the 2d position.

Each of four contours in Fig. 7e and 7f were generated from data of three heights, instead of four heights like the other conditions (cf. Fig. 6), due to occasional strong signal intensities that saturated some images at upper heights. This might have been attributed to the larger thermal power for 160 m/s air jet velocity cases combined with good atomization performance for the injector position of 1d (e.g., Fig. 7e). On the other hand, the rich flame condition was the reason for the strong signal for Fig. 7f cases.

According to the results and evaluations presented, the 3D-printed part has a clear impact on the atomization quality of the injection system. Therefore, its further effects on flame characteristics and burner performances are investigated by analyzing averaged OH* *CL* images. Since an extensive parameter study for the injection concept with a machined airblast has been done and presented by Hampp et al. [3], the current study focuses more on the comparison between the different airblasts.

From all pairs of the *CL* images (i.e., with the machined and the 3D-printed airblast), three pairs are presented in Fig. 8. A minor structural difference in the flame shape was observed from all pairs. As presented in the previous work [3], flames on this burner tend to have an elongated leading edge at the center of the burner tapering toward the nozzle. This phenomenon is well observed in the current study as well. However, with the 3D-printed airblast, the intensity of the leading edge gets weaker, so the flame shape becomes slightly broader and more symmetric. Less efficient atomization leading to a compactor flame shape is counter-intuitive, but the shortened leading edge with the 3D-printed airblast was observed from all the sets of 10 pairs and well presented in Fig. 8.

Apart from the general trend of the shortened leading edge, no significant change in the flame shape due to the larger droplet size was observed. For example, the averaged *CL* images presented in Fig. 8a are from the pair that shows the largest difference in the mean droplet size of the Jet A-1 liquid fuel (i.e., cases 3 and 13 in Fig. 7a). Even though the mean droplet size is about 25% (10 µm) larger with the 3D-printed airblast than with the machined airblast (cf. Fig. 7a), the corresponding *CL* images show similar intensity and spatial distribution of the OH radicals to each other. The similar *CL* images suggest no major influence in the flame shape and heat release zone attributed to the atomization performance change.

The other examples presented in Fig. 8b and 8c show the similar trend. Cases 8 and 18 have the largest droplet size difference for HEL (cf. Fig. 7b), and cases 9 and 19 are from the flames at the stoichiometric condition. The global structure of the flame does not present distinct dependencies on the type of airblast or spray characteristics.

Emission data from the burner has been analyzed and compared to find any possible indications of different flame behaviors. Nitrogen oxides (NOx) are especially of interest since they could indicate a flame temperature difference. For each flame condition, 60 data points (sampling rate of 1 Hz) of NOx and CO quantity, which were saved during the *CL* imaging, were averaged. The averaged values were corrected to 15% oxygen and plotted in Fig. 9 with their standard deviations.

From the NOx emission data in Fig. 9a, flames with the 3D-printed airblast tend to have slightly larger values for most of the cases than with the machined airblast. The difference is larger for the HEL flames, but not significantly. In addition, a relation between the NOx emission and the droplet size difference (cf. Fig. 5) is hard to establish. For example, large droplet size differences observed in Fig. 5 are pairs of cases 3-13, 5-15, and 10-20. On the other hand, large NOx emission differences in Fig. 9 are pairs of cases 6-16, 7-17, and 10-20.

CO emission data in Fig. 9 presents similar trend as the NOx emission data. For the cases with Jet A-1, no significant correlation between emission values an the airblast type is observed. HEL flames show more deviated values between the machined and the 3D-printed airblast cases. However, the difference is relatively small as less than 25 ppm for the ϕ=0.8 cases and 55 ppm for the ϕ=1 case. Despite the increased emission with the 3D-printed airblast, CO levels at all ϕ=0.8 conditions in this study are within the range of the reported typical CO emission level of gas turbines, which is between 5 and 330 ppm [16].

The large difference of CO emission levels is observed from the same pairs of the cases as the NOx emission result (i.e., 6-16, 7-17, and 10-20) with an addition of 9-19. Therefore, it is not correlated with the droplet size difference results, either. The NOx and CO emission levels are responding more sensitively to the flame conditions (air jet velocity and ϕ) than the type of airblast.

4. CONCLUSION

The series of tests with the machined and the 3D-printed airblast presents that the impact of the 3D-printed part on the atomization quality is not negligible. Droplet size distribution clearly changes toward a larger value with the 3D-printed airblast, and a larger number of droplets are detected as well. Therefore, it is concluded that the atomization with the 3D-printed airblast is less efficient than the conventionally machined airblast, due to the interaction between the liquid and the rough surface.

On the other hand, the less efficient atomization does not affect much negatively on the flame behavior in this burner. No significant change in the flame position and intensity has been observed, and the emission profile stayed stable as well. This can be attributed to the robust burner system that can stabilize flames under a wide operation range. Therefore, it was concluded that employing the 3D printed components to the burner system would provide comparable combustion characteristics while giving significant benefits by realizing challenging geometry, reducing time for manufacturing, and saving cost.

Nevertheless, multiple trends and phenomena are observed during this study and require further investigation. An example is the interaction between a liquid fuel and a 3D-printed surface and how it affects the atomization performance of an injection system. Fundamental studies to answer the questions will help find the boundary of the operational range of the current burner system with 3D-printed components, which would further serve to optimize the combustor.

ACKNOWLEDGMENT

The authors would like to thank Fabian Hampp and Yeonse Kang for supporting this work with preparations and discussions and also Manuel Löber for the help with the secondary electron imaging of the airblast surfaces.

NOMENCLATURE

CL	Chemiluminescence
FN	Flow Number (US)
HEL	Extra Light Heating Oil
MGT	Micro Gas Turbine
ϕ	Equivalence Ratio
PSA	Pressure Swirl Atomizer
SLM	Selective Laser Melting

REFERENCES

[1] Samitha Weerakoon, A.H., and Assadi, M., 2023, "Trends and advances in micro gas turbine technology for sustainable energy solutions: A detailed review," Energy Conversion and Management: X **20**, 100483. DOI: 10.1016/j.ecmx.2023.100483

[2] Enagi, I.I., Al-attab, K.A., Zainal, Z.A., and Teoh, Y.H., 2022, "Palm biodiesel spray and combustion characteristics in a new micro gas turbine combustion chamber design," Energy **254**, 124335. DOI: 10.1016/j.energy.2022.124335

[3] Hampp, F., Schäfer, D., and Lammel, O., 2023, "Spray flame characterization of a dual injector for compact combustion systems," Combustion Science and Technology. DOI: 10.1080/00102202.2023.2249222

[4] Giuliani, F., Paulitsch, N., Cozzi, D., Görtler, M., and Andracher, L., 2018, "An assessment on the benefits of additive manufacturing regarding new swirler geometries for gas turbine burners," Proceedings of the ASME Turbo Expo **4A**. DOI: 10.1115/GT2018-75165

[5] Novotny, V., Spale, J., Bryksi Stunova, B., Kolovratnik, M., Vitvarova, M., and Zikmund, P., 2019, "3D printing in turbomachinery: Overview of technologies, applications and possibilities for industry 4.0," Proceedings of the ASME Turbo Expo **6**. DOI: 10.1115/GT2019-91849

[6] Dahmen, T., 2021, "Additive manufacturing for fuel injectors: Design, processes and materials," Kgs. Lyngby: Technical University of Denmark

[7] Sanchez, F., Corber, A., and Barbacki, M., 2018, "Assessment of spray particle size on holes created through additive manufacturing methods (SLM) vs conventionally drilled," Proceedings of GPPS Forum **18**

[8] Wang, Z., Fan, W., Shi, H., Shi, P., and Don, R., 2022, "Study of atomization characteristics of air atomizing nozzles for additive manufacturing," Journal of Physics: Conference Series **2228**, 012032. DOI: 10.1088/1742-6596/2228/1/012032

[9] Cejpek, O., Malý, M., Bělka, M., and Jedelský, J., 2020, "Replication of pressure swirl atomizer by 3D printing and influence of surface roughness on the atomization quality," MATEC Web of Conferences **328**, 01007. DOI: 10.1051/matecconf/202032801007

[10] Jedelský, J., Malý, M., Bělka, M., Polzer, A., Sámelová, V., Cejpek, O., and Wigley, G., 2023, "Effect of fabrication method and surface roughness on spray characteristics for small pressure-swirl atomizers," Journal of Manufacturing Processes **85**, pp. 166-178. DOI: 10.1016/j.jmapro.2022.11.031

[11] Crayford, A.P., Lacan, F., Runyon, J., Bowen, P.J., Balwadkar, S., Harper, J., and Pugh, D.G., 2019, "Manufacture, characterization and stability limits of an AM prefilming air-blast atomizer," Proceedings of the ASME Turbo Expo **4B**. DOI: 10.1115/GT2019-91624

[12] Lammel, O., Stöhr, M., Kutne, P., Dem, C., Meier, W., and Aigner, M., 2012, "Experimental analysis of confined jet flames by laser measurement techniques," Journal of Engineering for Gas Turbines and Power **134**(4), 041506. DOI: 10.1115/1.4004733

[13] Lefebvre, A.H., and McDonell, V.G., 2017, *Atomization and sprays* (2nd ed.), CRC press. DOI: 10.1201/9781315120911

[14] Allan, D.B., Caswell, T., Keim, N.C., van der Wel, C.M., and Verweij, R.W., 2023, *Trackpy* v0.6.1, Zenodo

[15] Crocker, J.C., and Grier, D.G., 1996, "Methods of digital video microscopy for colloidal studies," Journal of Colloid and Interface Science **179**(1), pp. 298–310. DOI: 10.1006/jcis.1996.0217

[16] Pavri, R., and Moore, G.D., 2001, "Gas turbine emissions and control," General Electric Report, No. GER-4211

Figure List

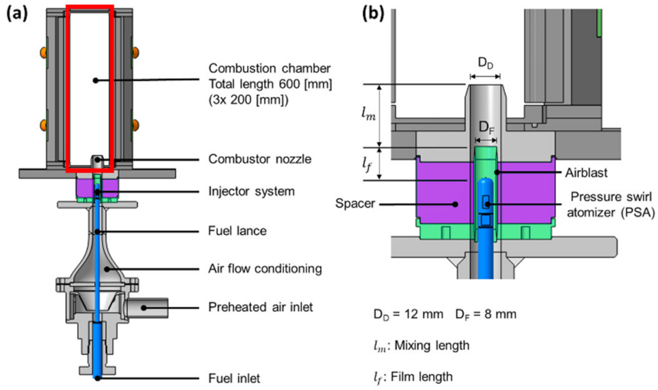

Fig. 1 SCHEMATIC of a confined jet-stabilized burner and details of a pressure swirl-airblast liquid fuel injection system [3]. The region in the red box (a) is utilized for the legends in Fig. 4, 5, and 6.

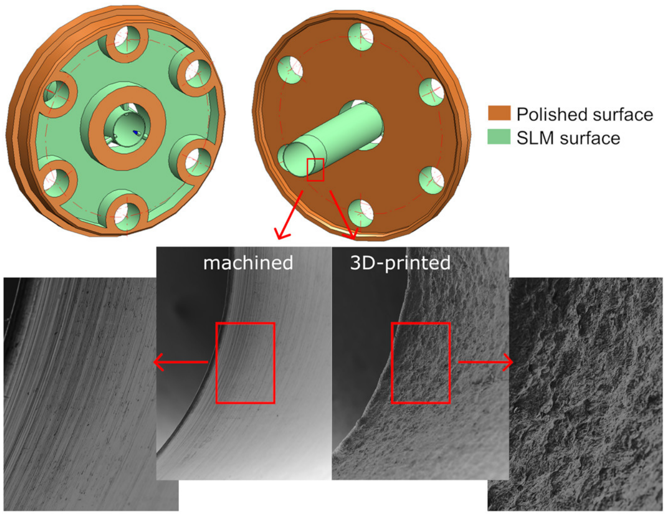

Fig. 2 3D model and microscopic images of the machined and 3d-printed airblast

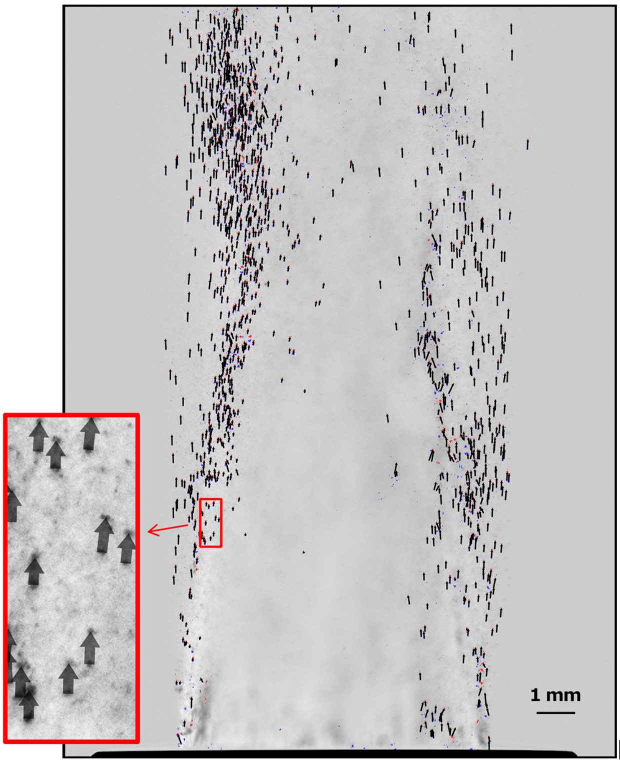

Fig. 3 SAMPLE shadowgraphy image overlaid by a particle tracking result. Two frames are taken with a time interval of 2 µs at the height close to the nozzle for case nr. 6 (cf. Table 1) condition. Vectors indicate the displacement of detected particles.

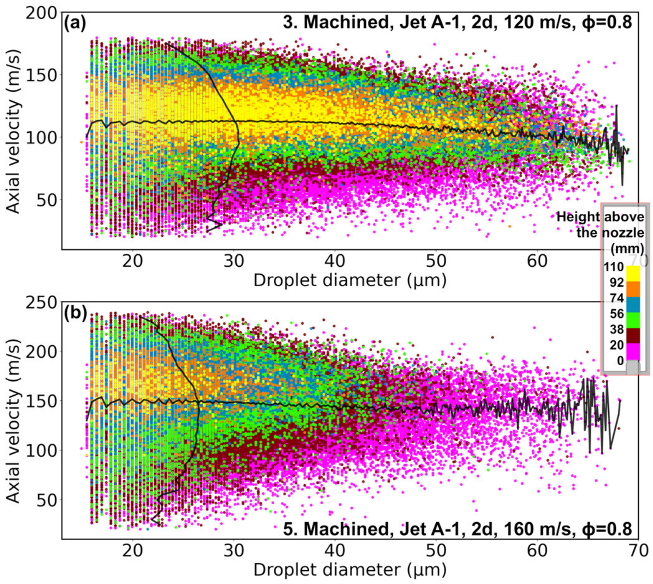

Fig. 4 VELOCITY-SIZE scatter plots of detected Jet A-1 droplets. Air jet velocities of 120 m/s (case nr. 3) and 160 m/s (case nr. 5) are compared, with the machined airblast and PSA located at 2d below the nozzle tip. Mean group velocities (horizontal) and mean group sizes (vertical) of all detected

droplets are drawn with the black lines. The mean curves of each height are presented in Fig. 5.

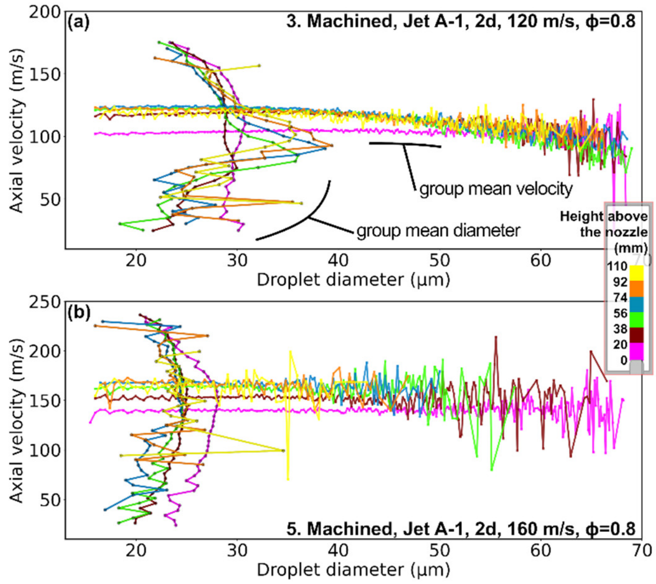

Fig. 5 GROUP mean velocity and group mean size plots of detected Jet A-1 droplets. Air jet velocities of 120 m/s (case nr. 3) and 160 m/s (case nr. 5) are compared, with the machined airblast and PSA located at 2d below the nozzle tip. Data points of individual droplets are presented in Fig. 4.

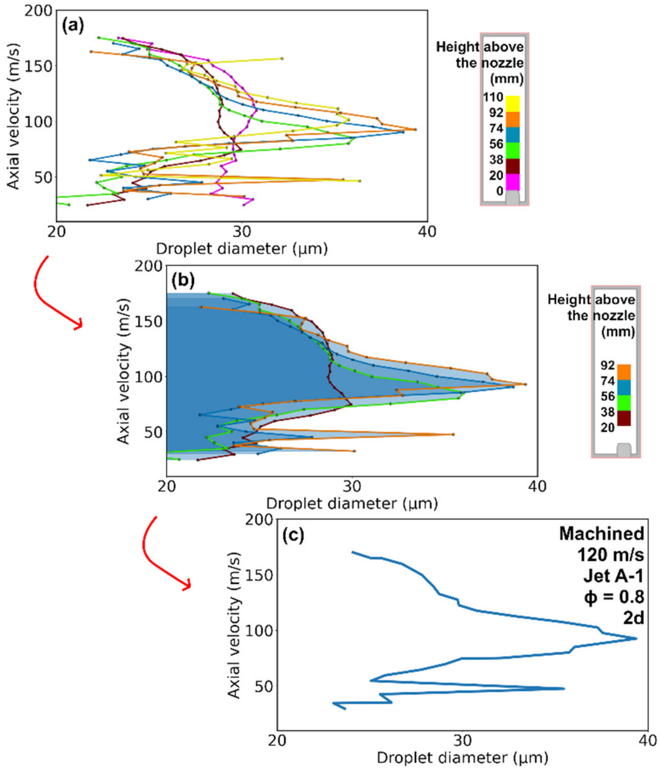

Fig. 6 ILLUSTRATION of drawing contours using grouped mean droplet size curves. Vertical lines of a sample case (case

nr. 3) in Fig. 5 are presented (a), four central heights are selected, and the area under the curves is filled with blue (b). A contour of the filled area is drawn with blue (c). The blue contour can be found in Fig. 7a and 7c.

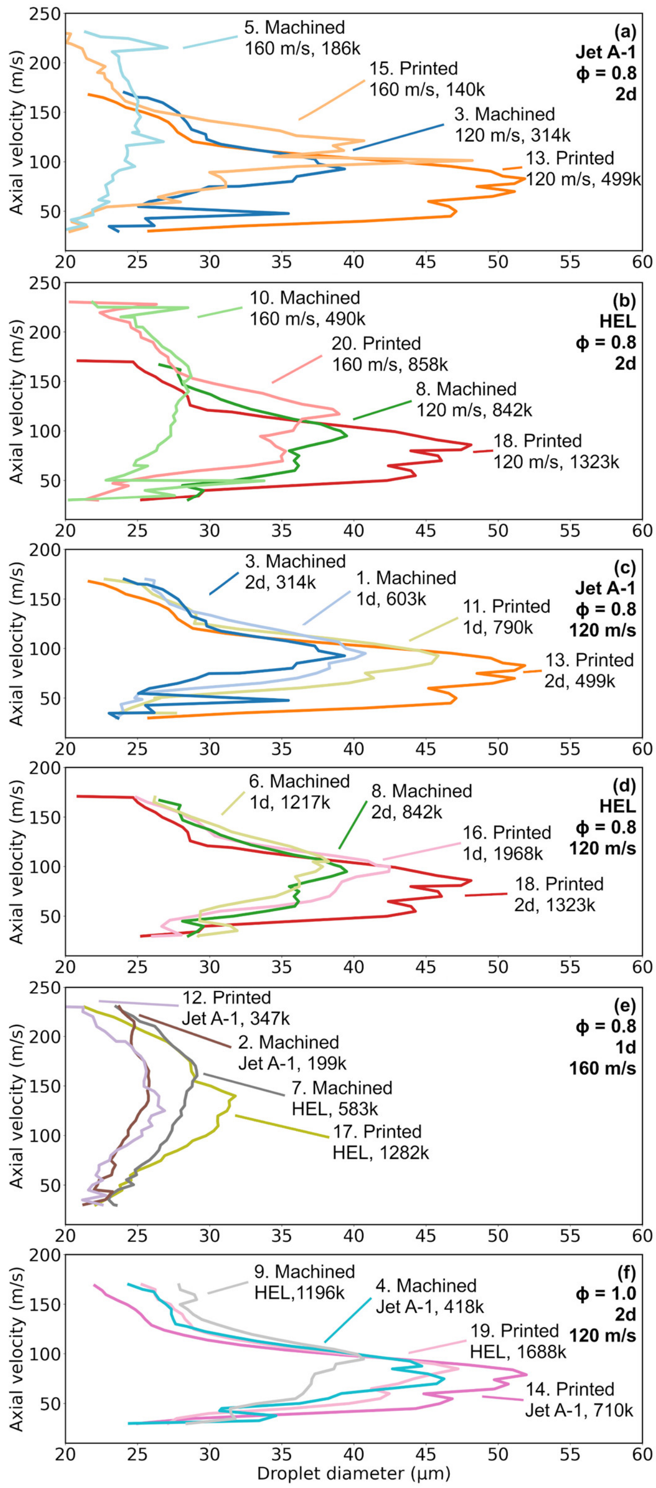

451 Fig. 7 ATOMIZATION performance
452 analysis at various conditions using droplet size contours. Droplet size contours of
453 various cases are compared (cf. Fig. 6). Shared parameters within one panel are noted at
454 the upper right corners, and individual parameters are noted with the case numbers

from Table 1, and the total number of droplets detected from each set of 300 images (e.g., 710k=710000 droplets).

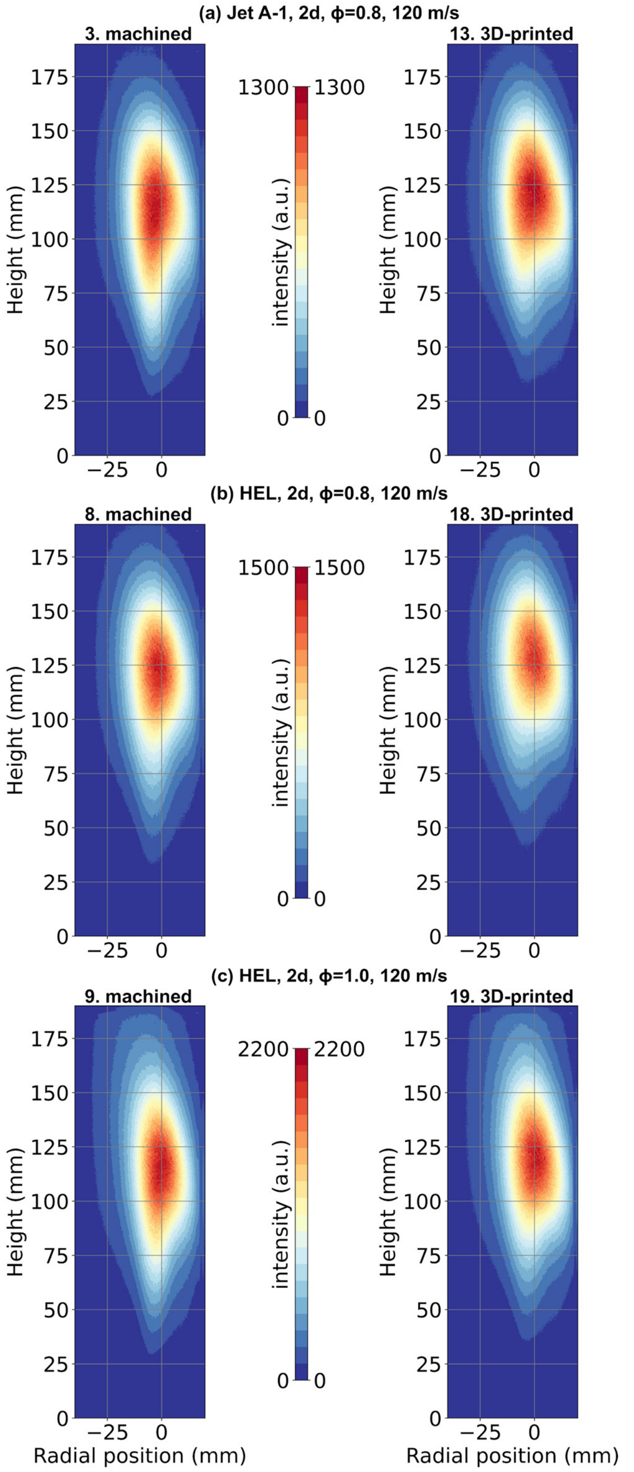

Fig. 8 AVERAGED OH* chemiluminescence images with the machined airblast and the 3D-printed airblast. Jet

A-1 flames are presented in panel a, and HEL flames are presented in panels b and c. Detailed parameters are noted in each panel. A discrete color scale with a 5% interval is used.

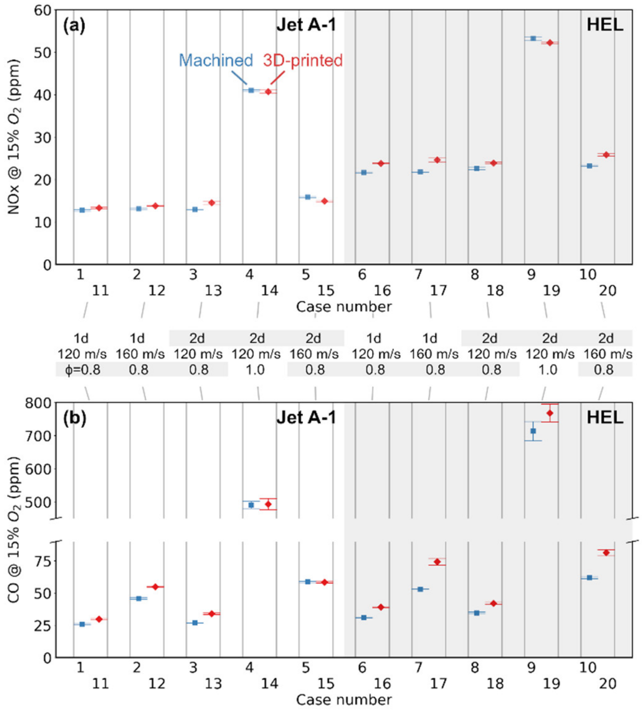

Fig. 9 EMISSION data of nitrogen oxides (NOx) and carbon monoxide (CO). Data points with the machined airblast (blue) and the 3D-printed airblast (red) are plotted together for comparison. Cases 1 to 5 on the left are the results of Jet A-1 flames, and cases 6 to 10 on the right are with HEL as a liquid fuel. Standard deviation of each data point is represented by error bars.

Table Caption List

Table 1 EXPERIMENTAL conditions of the study

TABLE 1: EXPERIMENTAL conditions of the study

Fuel	Injector position	Air jet vel. (m/s)	ϕ	Case nr. (Airblast type)	
				Machined	Printed
Jet A-1	1d	120	0.8	1	11
		160	0.8	2	12
	2d	120	0.8	3	13
			1.0	4	14
		160	0.8	5	15
HEL	1d	120	0.8	6	16
		160	0.8	7	17
	2d	120	0.8	8	18
			1.0	9	19
		160	0.8	10	20